INTERNATIONAL JOURNAL FOR NUMERICAL METHODS IN FLUIDS
Int. J. Numer. Meth. Fluids 2008; **57**:1321–1348
Published online in Wiley InterScience (www.interscience.wiley.com). DOI: 10.1002/fld.1842

A stabilized mixed finite element method for the first-order form of advection–diffusion equation

Arif Masud*, †, ‡ and JaeHyuk Kwack§

Department of Civil and Environmental Engineering, University of Illinois at Urbana-Champaign, 3110 Newmark Civil Engineering Laboratory, MC-250, Urbana, IL 61801-2352, U.S.A.

SUMMARY

This paper presents a stabilized mixed finite element method for the first-order form of advection–diffusion equation. The new method is based on an additive split of the flux-field into coarse- and fine-scale components that systematically lead to coarse and fine-scale variational formulations. Solution of the fine-scale variational problem is mathematically embedded in the coarse-scale problem and this yields the resulting method. A key feature of the method is that the characteristic length scale of the mesh does not appear explicitly in the definition of the stability parameter that emerges via the solution of the fine-scale problem. The new method yields a family of equal- and unequal-order elements that show stable response on structured and unstructured meshes for a variety of benchmark problems. Copyright © 2008 John Wiley & Sons, Ltd.

Received 5 October 2007; Revised 5 April 2008; Accepted 10 April 2008

KEY WORDS: stabilized methods; multiscale methods; continuous fields of arbitrary order; advection–diffusion equation; equal- and unequal-order elements

1. INTRODUCTION

Advection–diffusion phenomena appear in many problems in physical sciences and engineering, and therefore an accurate modeling of this phenomenon has been a focus of research in the field of fluid mechanics. Advection-dominated diffusion processes are typically modeled via a scalar-valued advection diffusion equation that also serves as a vehicle to study the more advanced flow models, namely, the Navier–Stokes equations. For the advection-dominated case, this equation

*Correspondence to: Arif Masud, Department of Civil and Environmental Engineering, University of Illinois at Urbana-Champaign, 3110 Newmark Civil Engineering Laboratory, MC-250, Urbana, IL 61801-2352, U.S.A.
†E-mail: amasud@uiuc.edu
‡Associate Professor.
§Graduate Research Assistant.

Contract/grant sponsor: National Academy of Sciences; contract/grant number: NAS 7251-05-005

becomes hyperbolic and develops sharp features in the solution. Classical numerical methods for the advection-dominated cases result in non-convergent solutions. Specifically, methods that are based on the standard Galerkin finite element approach lack stability that manifests itself in terms of non-physical oscillations. Various approaches based on stabilized methods [1–6], space–time finite element methods [7, 8] and discontinuous Galerkin methods [9] have been proposed in the literature. For a review of various successful approaches for advection–diffusion equation, see Franca *et al.* [10] and references therein.

The present paper is an extension of our earlier efforts in developing stabilized/multiscale formulations for the advection–diffusion equation [5] and for the convective–diffusive heat transfer [11]. In the present paper we write the system in its first-order form via introduction of the flux of the scalar field as an additional unknown. This formulation is typically suited for many problems from engineering science where higher accuracy of the flux is important, namely, porous media flows where the scalar field represents pressure, and flux represents the velocity field. An interested reader is referred to a recent paper by Rajagopal [12] that presents a hierarchy of pressure–velocity models for flows of incompressible fluids through porous media. The proposed mixed form is also applicable to convective–diffusive heat transfer where the unknown scalar field and its flux represent temperature and temperature-flux, respectively. A first-order form of the convection–diffusion equation has been pursued in [13]. However, developing finite element approximations of these spaces, which satisfy the celebrated Babuska–Brezzi, or inf–sup, stability condition [14, 15], is a challenging task. A literature review reveals that several elegant solutions to this problem have been proposed (see Raviart and Thomas [16], Brezzi *et al.* [17–19], Nedelec [20, 21], and Thomas [22]). These discrete spaces have been used successfully in numerous applications. Good accuracy has been attained for both velocity and pressure, and mass conservation is achieved locally (i.e. element-wise) as well as globally. However, this approach also has its drawback: complexity. Different interpolations are required for pressure and velocity and implementation is particularly complicated in three dimensions. To overcome the compatibility condition typical of mixed methods, Hughes and colleagues introduced Streamline-Upwind-Petrov–Galerkin (SUPG) technique [4, 23] that turned out to be the forerunner of the more general stabilized finite element method called the Galerkin/Least-squares (GLS) method. In a relatively recent effort, Masud and Hughes [24] presented a new mixed stabilized method for Darcy equation that was extended to discontinuous Galerkin method in Hughes *et al*. [25] and Brezzi *et al.* [26], and to Darcy–Stokes equation in Masud [27].

One of the objectives of this paper is to demonstrate that using the first-order form of the advection–diffusion equation that leads to mixed methods, one can develop simple and robust stabilization techniques. We employ Hughes' variational multiscale method [28] with the underlying philosophy of strengthening the classical variational formulation so that discrete approximations, which would otherwise be unstable, become stable and convergent. An interesting aspect of the new variational formulation is that an explicit appearance of the characteristic length scale of the mesh does not take place in the structure of the stability parameter that has been derived via the solution of the fine-scale problem. This may be contrasted with most stabilized methods in which mesh-dependent parameters appear that may be thought of as arising from elimination of unresolved scales in a multiscale decomposition of the solution (see Hughes [28] and Hughes *et al.* [29] for elaboration).

An outline of the paper is as follows. Section 2 presents the boundary value problem for advection–diffusion equation that is written in its first-order form. Section 3 presents the standard weak form of the problem. Section 4 presents the new stabilized form that is derived based

DOI: 10.1002/fld

on multiscale decomposition of the velocity field. Numerical results are given in Section 5 and conclusions are drawn in Section 6.

2. THE FIRST-ORDER FORM OF THE ADVECTION–DIFFUSION EQUATION

Let $\Omega \subset \mathbb{R}^{n_{\mathrm{sd}}}$ be an open bounded region with piecewise smooth boundary Γ. The number of space dimensions, n_{sd}, is equal to 2 or 3. The advection–diffusion equation can be written in the first-order form as

$$\frac{1}{\kappa}\mathbf{v} = \frac{1}{\kappa}\boldsymbol{\alpha} p - \nabla p \quad \text{on } \Omega \tag{1}$$

$$\operatorname{div} \mathbf{v} = \varphi \quad \text{on } \Omega \tag{2}$$

where p is the scalar unknown field that in the present context is considered as the pressure field, $\mathbf{v}$ is the flux-field that is considered as the velocity field, $\boldsymbol{\alpha}$ is the given advective flow field, assumed solenoidal, i.e. $\nabla \cdot \boldsymbol{\alpha} = 0$. κ is the diffusion parameter and φ is the source term. We split the total flux into advective and diffusive parts $\mathbf{v} = \mathbf{v}^{\mathrm{a}} + \mathbf{v}^{\mathrm{d}}$, where $\mathbf{v}^{\mathrm{a}} = \boldsymbol{\alpha} p$ is the advective velocity, and $\mathbf{v}^{\mathrm{d}} = -\kappa \nabla p$ is the diffusive velocity.

We define the normal component of the given advective flow as $\alpha_n = \mathbf{n} \cdot \boldsymbol{\alpha}$, where $\mathbf{n}$ is the unit outward normal to Γ. Let $\{\Gamma^-, \Gamma^+\}$ and $\{\Gamma_g, \Gamma_h\}$ be the partitions of Γ, where $\Gamma^- = \{\mathbf{x} \in \Gamma \,|\, \alpha_n(\mathbf{x}) < 0\}$ is the inflow boundary, and $\Gamma^+ = \Gamma - \Gamma^-$ is the outflow boundary. Consequently, part of the boundary where Dirichlet boundary conditions are specified is further split into inflow and outflow Dirichlet boundaries, defined as $\Gamma_g^{\pm} = \Gamma_g \cap \Gamma^{\pm}$. Similarly, part of the boundary where Neumann boundary conditions are specified is also further split into inflow and outflow Neumann boundaries, defined as $\Gamma_h^{\pm} = \Gamma_h \cap \Gamma^{\pm}$. With the definitions of the inflow and outflow boundaries given above, the given normal advective flow field on the inflow boundary Γ^- is expressed as $\alpha_n^- = (\alpha_n - |\alpha_n|)/2$; and given normal advective flow field on the outflow boundary Γ^+ is expressed as $\alpha_n^+ = (\alpha_n + |\alpha_n|)/2$.

To the governing equations (1) and (2), we add the following boundary conditions:

$$\mathbf{v} \cdot \mathbf{n} = \psi^- \quad \text{on } \Gamma_{g_v}^- \quad \text{(velocity boundary condition on inflow)} \tag{3a}$$

$$\mathbf{v}^{\mathrm{d}} \cdot \mathbf{n} = \psi^+ \quad \text{on } \Gamma_{g_v}^+ \quad \text{(velocity boundary condition on outflow)} \tag{3b}$$

$$p = g \quad \text{on } \Gamma_{g_p} \quad \text{(pressure boundary condition)} \tag{4}$$

where (3a) and (3b) represent the total normal velocity and the diffusive normal velocity conditions on the inflow and the outflow Dirichlet boundaries, respectively. Accordingly, ψ^- is the prescribed normal total velocity on the inflow, ψ^+ is the prescribed normal diffusive velocity on the outflow Dirichlet boundaries, and g is the prescribed pressure boundary condition on Γ_{g_p}.

3. WEAK FORM OF THE PROBLEM

The appropriate spaces of functions for the velocity and the pressure fields are $\mathbf{H}(\operatorname{div}, \Omega)$ and $L_2(\Omega)$, respectively. $\mathbf{H}(\operatorname{div}, \Omega)$ is the space of Lebesgue square-integrable vector fields whose divergence is also Lebesgue square-integrable. $L_2(\Omega)$ is the space of Lebesgue square-integrable

DOI: 10.1002/fld

functions defined on the domain Ω. For a detailed exposition on the functional spaces, see Brezzi and Fortin [30].

Let

$$\mathbf{H}(\mathrm{div},\Omega)=\{\mathbf{v}|\mathbf{v}\in(L_2(\Omega))^{\mathrm{nsd}},\mathrm{div}\,\mathbf{v}\in L_2(\Omega),\mathrm{trace}(\mathbf{v}\cdot\mathbf{n})=\psi^-\in H^{-1/2}(\Gamma_{g_v}^-)\} \tag{5}$$

$$\mathscr{S}=\{\mathbf{v}|\mathbf{v}\in\mathbf{H}(\mathrm{div},\Omega),\mathbf{v}\cdot\mathbf{n}=\psi^-\text{ on }\Gamma_{g_v}^-,\mathbf{v}^{\mathrm{d}}\cdot\mathbf{n}=\psi^+\text{ on }\Gamma_{g_v}^+\} \tag{6a}$$

$$\mathscr{V}=\{\mathbf{w}|\mathbf{w}\in\mathbf{H}(\mathrm{div},\Omega),\mathbf{w}\cdot\mathbf{n}=0\text{ on }\Gamma_{g_v}^-\} \tag{6b}$$

$$\mathscr{P}=\left\{p|p\in L_2(\Omega),p=g\text{ if }\Gamma_{g_p}\neq\emptyset,\int_\Omega p\,\mathrm{d}\Omega=0\text{ if }\Gamma_{g_p}=\emptyset\right\} \tag{6c}$$

The formal statement is: Find $\mathbf{v}\in\mathscr{S}$, $p\in\mathscr{P}$ such that for all $\mathbf{w}\in\mathscr{V}$, $q\in\mathscr{P}$

$$\left(\mathbf{w},\frac{1}{\kappa}\mathbf{v}\right)-\left(\mathbf{w},\frac{1}{\kappa}\boldsymbol{\alpha}p\right)-(\mathrm{div}\,\mathbf{w},p)+(q,\mathrm{div}\,\mathbf{v})+\left(\mathbf{w}\cdot\mathbf{n},\frac{1}{\alpha_n}\mathbf{v}\cdot\mathbf{n}\right)_{\Gamma_{g_v}^+}=(q,\varphi)+\left(\mathbf{w}\cdot\mathbf{n},\frac{1}{\alpha_n}\psi^+\right)_{\Gamma_{g_v}^+} \tag{7}$$

where $(\cdot,\cdot)=\int_\Omega(\cdot)\,\mathrm{d}\Omega$ is the $L_2(\Omega)$—inner product.

We write the standard weak form in an abstract form: Find $\mathbf{V}=\{\mathbf{v},p\}\in\mathscr{S}\times\mathscr{P}$ such that, for all $\mathbf{W}=\{\mathbf{w},q\}\in\mathscr{V}\times\mathscr{P}$,

$$B(\mathbf{W},\mathbf{V})=L(\mathbf{W}) \tag{8}$$

$$B(\mathbf{W},\mathbf{V})=\left(\mathbf{w},\frac{1}{\kappa}\mathbf{v}\right)-\left(\mathbf{w},\frac{1}{\kappa}\boldsymbol{\alpha}p\right)-(\mathrm{div}\,\mathbf{w},p)+(q,\mathrm{div}\,\mathbf{v})+\left(\mathbf{w}\cdot\mathbf{n},\frac{1}{\alpha_n}\mathbf{v}\cdot\mathbf{n}\right)_{\Gamma_{g_v}^+} \tag{9}$$

$$L(\mathbf{W})=(q,\varphi)+\left(\mathbf{w}\cdot\mathbf{n},\frac{1}{\alpha_n}\psi^+\right)_{\Gamma_{g_v}^+} \tag{10}$$

Remark 1

Equation (7) presents the mixed weak form of the problem. It is well documented that within the framework of standard Galerkin method only certain combinations of velocity and pressure interpolations are stable. In the following sections we will develop a modified formulation that is inherently more stable and therefore accommodates arbitrary velocity–pressure interpolations that are convenient from a practical implementation view point.

4. THE VARIATIONAL MULTISCALE METHOD

We consider discretization of the domain into non-overlapping subregions/elements. The sum of the interiors of these subregions/elements is indicated as Ω', and sum over element boundaries is

DOI: 10.1002/fld

indicated as Γ':

$$\Omega' = \bigcup_{e=1}^{n_{\text{umel}}} (\text{int})\Omega^e \quad \text{(elem. interiors)} \tag{11a}$$

$$\Gamma' = \bigcup_{e=1}^{n_{\text{umel}}} \Gamma^e \quad \text{(elem. boundaries)} \tag{11b}$$

We assume an overlapping additive decomposition of the velocity field into coarse or resolvable scales, and fine or subgrid scales. Likewise, we assume a similar sum decomposition of the weighting function into coarse and fine scales, and consider the case where $\mathbf{v}'(\mathbf{x}) = \mathbf{w}'(\mathbf{x}) = \mathbf{0}$ on Γ':

$$\mathbf{v}(\mathbf{x}) = \underbrace{\overline{\mathbf{v}}(\mathbf{x})}_{\text{coarse scale}} + \underbrace{\mathbf{v}'(\mathbf{x})}_{\text{fine scale}} \tag{12}$$

$$\mathbf{w}(\mathbf{x}) = \underbrace{\overline{\mathbf{w}}(\mathbf{x})}_{\text{coarse scale}} + \underbrace{\mathbf{w}'(\mathbf{x})}_{\text{fine scale}} \tag{13}$$

Remark 2
The assumption that fine scales vanish at the inter element boundaries helps in keeping the presentation of ideas simple. However, it is not a limitation of the present method. Relaxing this restriction would require Lagrange multipliers to enforce the inter element continuity of the fine-scale fields [31].

We substitute (12) and (13) into (7) and this leads to a modified variational form.

$$\begin{aligned}\left(\overline{\mathbf{w}}+\mathbf{w}', \frac{1}{\kappa}(\overline{\mathbf{v}}+\mathbf{v}')\right) - \left(\overline{\mathbf{w}}+\mathbf{w}', \frac{1}{\kappa}\boldsymbol{\alpha}p\right) - (\operatorname{div}(\overline{\mathbf{w}}+\mathbf{w}'), p) + (q, \operatorname{div}(\overline{\mathbf{v}}+\mathbf{v}')) \\ + \left((\overline{\mathbf{w}}+\mathbf{w}')\cdot\mathbf{n}, \frac{1}{\alpha_n}(\overline{\mathbf{v}}+\mathbf{v}')\cdot\mathbf{n}\right)_{\Gamma^+_{gv}} = (q, \varphi) + \left((\overline{\mathbf{w}}+\mathbf{w}')\cdot\mathbf{n}, \frac{1}{\alpha_n}\psi^+\right)_{\Gamma^+_{gv}}\end{aligned} \tag{14}$$

Using the linearity of the weighting function slot we can split (14) into a coarse-scale problem (15), and a fine-scale problem (16). Employing the condition that $\mathbf{v}'(\mathbf{x}) = \mathbf{w}'(\mathbf{x}) = \mathbf{0}$ on Γ' we get

Coarse-scale problem:

$$\begin{aligned}\left(\overline{\mathbf{w}}, \frac{1}{\kappa}(\overline{\mathbf{v}}+\mathbf{v}')\right) - \left(\overline{\mathbf{w}}, \frac{1}{\kappa}\boldsymbol{\alpha}p\right) - (\operatorname{div}\overline{\mathbf{w}}, p) + (q, \operatorname{div}(\overline{\mathbf{v}}+\mathbf{v}')) \\ + \left(\overline{\mathbf{w}}\cdot\mathbf{n}, \frac{1}{\alpha_n}\overline{\mathbf{v}}\cdot\mathbf{n}\right)_{\Gamma^+_{gv}} = (q, \varphi) + \left(\overline{\mathbf{w}}\cdot\mathbf{n}, \frac{1}{\alpha_n}\psi^+\right)_{\Gamma^+_{gv}}\end{aligned} \tag{15}$$

Fine-scale problem:

$$\left(\mathbf{w}', \frac{1}{\kappa}(\overline{\mathbf{v}}+\mathbf{v}')\right) - \left(\mathbf{w}', \frac{1}{\kappa}\boldsymbol{\alpha}p\right) - (\operatorname{div}\mathbf{w}', p) = 0 \tag{16}$$

DOI: 10.1002/fld

4.1. Solution of the fine-scale problem

We first consider the fine-scale problem given by Equation (16), which, because of the assumption on the fine-scale field, is defined over Ω'. Our objective is to solve (16) and extract the fine-scale flux field $\mathbf{v}'$ that can then be substituted into (15) thereby eliminating the explicit appearance of $\mathbf{v}'$ in the coarse-scale problem (15) while modeling the effects of the fine scales.

We keep the fine-scale velocity term on the left-hand side of (16) and take all the remaining terms to the right-hand side:

$$\left(\mathbf{w}', \frac{1}{\kappa}\mathbf{v}'\right)_{\Omega'} = -\left(\mathbf{w}', \frac{1}{\kappa}\overline{\mathbf{v}}\right)_{\Omega'} + \left(\mathbf{w}', \frac{1}{\kappa}\boldsymbol{\alpha}p\right)_{\Omega'} + (\operatorname{div}\mathbf{w}', p)_{\Omega'} \tag{17}$$

where $(\cdot,\cdot)_{\Omega'} = \sum_{e=1}^{\text{numel}} \int_{\Omega^e} (\cdot)\,\mathrm{d}\Omega$ is the $L_2(\Omega')$ inner product.

Applying integration-by-parts to the third term on the right-hand side of (17), employing condition that $\mathbf{v}' = \mathbf{w}' = \mathbf{0}$ on Γ' and then combining the terms we see that the fine-scale problem is driven by the residual of the flux form of the Euler–Lagrange equation (1). It can be written in a concise form as

$$(\mathbf{w}', \mathbf{v}')_{\Omega'} = -(\mathbf{w}', \overline{\mathbf{r}})_{\Omega'} \tag{18}$$

where $\overline{\mathbf{r}}$ is the residual defined as $\overline{\mathbf{r}} = \overline{\mathbf{v}} - \boldsymbol{\alpha}p + \kappa\nabla p$. At this point one can employ either the Greens function approach [28, 29] or the bubble function approach [3, 32] to solve (18). Equivalence between the two approaches has been established in [33]. Following our earlier efforts in [5, 34, 35], we adopt the bubble function approach and expand fine-scale fields as follows:

$$\mathbf{v}'|_{\Omega^e} = b^e(\boldsymbol{\xi})\boldsymbol{\beta} \tag{19a}$$

and

$$\mathbf{w}'|_{\Omega^e} = b^e(\boldsymbol{\xi})\boldsymbol{\gamma} \tag{19b}$$

where $b^e(\boldsymbol{\xi})$ represents the bubble function, $\boldsymbol{\beta}$ represents the coefficients for the fine-scale velocity field, and $\boldsymbol{\gamma}$ represents the coefficients for the fine-scale weighting function. Substituting (19a) and (19b) into (18), taking the constant coefficients out of the integral expression, and assuming that the projection of the coarse-scale residual over the element interiors is constant, we get

$$\boldsymbol{\gamma}\left[\int_{\Omega^e} (b^e)^2\,\mathrm{d}\Omega\right]\boldsymbol{\beta} = -\boldsymbol{\gamma}\left(\int_{\Omega^e} b^e\,\mathrm{d}\Omega\right)\overline{\mathbf{r}} \tag{20}$$

Solving (20) for the fine-scale coefficients $\boldsymbol{\beta}$, the fine-scale field $\mathbf{v}'$ can be reconstructed via recourse to Equation (19a) as

$$\begin{aligned}\mathbf{v}'(\mathbf{x}) &= -\tau\overline{\mathbf{r}} \\ &= -\tau(\overline{\mathbf{v}} - \boldsymbol{\alpha}p + \kappa\nabla p)\end{aligned} \tag{21}$$

where the stability parameter τ is defined as

$$\tau = b^e\left(\int_{\Omega^e} (b^e)^2\,\mathrm{d}\Omega\right)^{-1}\int_{\Omega^e} b^e\,\mathrm{d}\Omega \tag{22}$$

DOI: 10.1002/fld

4.2. Solution of the coarse-scale problem

With the expression for the fine scales obtained in (21) we reconsider the coarse-scale problem given by (15). Applying integration-by-parts to the fine-scale component from the fourth term on the left-hand side of (15) and then by combining the fine-scale terms, we get

$$\left(\overline{\mathbf{w}}, \frac{1}{\kappa}\overline{\mathbf{v}}\right) - \left(\overline{\mathbf{w}}, \frac{1}{\kappa}\boldsymbol{\alpha} p\right) - (\operatorname{div}\overline{\mathbf{w}}, p) + (q, \operatorname{div}\overline{\mathbf{v}}) + \left(\frac{1}{\kappa}\overline{\mathbf{w}} - \nabla q, \mathbf{v}'\right) + \left(\overline{\mathbf{w}}\cdot\mathbf{n}, \frac{1}{\alpha_n}\overline{\mathbf{v}}\cdot\mathbf{n}\right)_{\Gamma_{g_v}^+} = (q, \varphi) + \left(\overline{\mathbf{w}}\cdot\mathbf{n}, \frac{1}{\alpha_n}\psi^+\right)_{\Gamma_{g_v}^+} \tag{23}$$

Substituting $\mathbf{v}'$ from (21) and then substituting the residual $\overline{\mathbf{r}} = \overline{\mathbf{v}} - \boldsymbol{\alpha} p + \kappa \nabla p$, we get the coarse-scale formulation:

$$\left(\overline{\mathbf{w}}, \frac{1}{\kappa}\overline{\mathbf{v}}\right) - \left(\overline{\mathbf{w}}, \frac{1}{\kappa}\boldsymbol{\alpha} p\right) - (\operatorname{div}\overline{\mathbf{w}}, p) + (q, \operatorname{div}\overline{\mathbf{v}}) + \left(\overline{\mathbf{w}}\cdot\mathbf{n}, \frac{1}{\alpha_n}\overline{\mathbf{v}}\cdot\mathbf{n}\right)_{\Gamma_{g_v}^+} - \left(\frac{1}{\kappa}\overline{\mathbf{w}} - \nabla q, \tau(\overline{\mathbf{v}} - \boldsymbol{\alpha} p + \kappa \nabla p)\right)_{\widetilde{\Omega}} = (q, \varphi) + \left(\overline{\mathbf{w}}\cdot\mathbf{n}, \frac{1}{\alpha_n}\psi^+\right)_{\Gamma_{g_v}^+} \tag{24}$$

It is important to note that Equation (24) is written completely in terms of the coarse-scale fields, whereas the fine-scale flux is now being modeled via the sixth integral on the left-hand side of (24).

4.3. The stabilized mixed form

We define the admissible space of functions for the pressure field

$$\mathscr{Q} = H^1(\Omega) = \left\{ p \,|\, p \in L_2(\Omega), \nabla p \in (L_2(\Omega))^{\mathrm{nsd}}, p = g \text{ if } \Gamma_{g_p} \neq \emptyset, \int_\Omega p \, \mathrm{d}\Omega = 0 \text{ if } \Gamma_{g_p} = \emptyset \right\} \tag{25}$$

The stabilized/multiscale mixed form is: Find $\mathbf{V} \in \mathscr{S} \times \mathscr{Q}$ such that, for all $\mathbf{W} \in \mathscr{V} \times \mathscr{Q}$,

$$B_{\mathrm{stab}}(\mathbf{W}, \mathbf{V}) = L_{\mathrm{stab}}(\mathbf{W}) \tag{26}$$

where the bilinear form $B_{\mathrm{stab}}(\mathbf{W}, \mathbf{V})$ and the linear form $L_{\mathrm{stab}}(\mathbf{W})$ are presented as follows:

$$B_{\mathrm{stab}}(\mathbf{W}, \mathbf{V}) = B(\mathbf{W}, \mathbf{V}) + \left(\left(-\frac{1}{\kappa}\mathbf{w} + \nabla q\right), \tau(\mathbf{v} - \boldsymbol{\alpha} p + \kappa \nabla p)\right) \tag{27}$$

$$L_{\mathrm{stab}}(\mathbf{W}) = L(\mathbf{W}) \tag{28}$$

and $B(\mathbf{W}, \mathbf{V})$ and $L(\mathbf{W})$ are given by (9) and (10), respectively.

Remark 3

The new stabilized form given in (26)–(28) is different from the SUPG and GLS stabilized forms as well as the form obtained based on adjoint-stabilization concepts.

DOI: 10.1002/fld

Remark 4

An interesting aspect of the new variational formulation is that the definition of the stabilization parameter derived in (22) is free of the explicit appearance of the characteristic length scale of the mesh. This may be contrasted with most stabilized methods in which mesh-dependent parameters appear that may be thought of as arising from elimination of unresolved scales in a multiscale decomposition of the solution (see [28, 29] for elaboration).

Remark 5

If we set $\boldsymbol{\alpha}=\mathbf{0}$ in (27), we recover the stabilized mixed continuous form for the Darcy flow equations presented in [24].

4.4. Design of bubble functions for the first-order from of advection–diffusion equation

This section presents derivation of bubble functions for the first-order form of the advection–diffusion equation. The stabilization parameter τ for the second-order form of the advection–diffusion equation presented in Hughes *et al.* [7], Franca *et al.* [10], and Harari *et al.* [36] is order $O(h/|\boldsymbol{\alpha}|)$ in the advection-dominated case, i.e. for high Peclet number flows. However, for the diffusion-dominated case where Peclet number $Pe\leqslant 1$, stabilization parameter τ is order $O(h^2/\kappa)$. Our objective is to design bubble functions that yield stabilization parameter τ that asymptotes to a value of $\tau=0.5$ for $\boldsymbol{\alpha}=\mathbf{0}$, which in the present context is the Darcy limit proposed in [24]. For the advection-dominated case, we want that stabilization parameter asymptotes to $\tau\simeq 1$, which is the value attained in (22). In the following we design bubble functions that when substituted in (22) yield the desired behavior of τ that is shown in Figure 1 and is given by the following equation:

$$\tau(Pe)=-\frac{a}{Pe+2a}+1 \tag{29}$$

where a is the slope of the curve at $Pe=0$.

The design conditions for the bubble function $b^e(\boldsymbol{\xi})$ for one-dimensional problem are

$$\text{For } |\boldsymbol{\alpha}|h/\kappa=0,\ \tau=\tfrac{1}{2};\quad \text{Darcy limit } (\boldsymbol{\alpha}=\mathbf{0}\Rightarrow Pe=0) \tag{30}$$

$$\text{For } |\boldsymbol{\alpha}|h/\kappa\gg 1,\ \tau\simeq 1;\quad \text{Advection-dominated limit } (Pe\gg 1) \tag{31}$$

Let us assume the function to be of the form

$$b^e=(1-\xi^2)^n,\quad n>0 \tag{32}$$

and employ the following two design conditions:

$$b^e(\xi=\pm 1)=0\quad\text{and}\quad \max b^e(\xi)=1,\quad \xi\in[-1,1]\ \text{(normalization)} \tag{33}$$

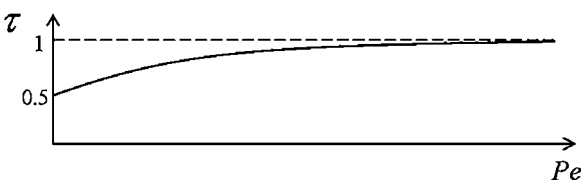

Figure 1. Stabilization parameter τ as a function of Pe.

DOI: 10.1002/fld

With the objective of economizing the cost of computation, we employ an average value of the function τ over the element. Consequently, Equation (22) becomes

$$\tau_{\text{avg}} = \frac{1}{\text{meas}(\Omega^e)} \int_{\Omega^e} \tau \, \mathrm{d}\Omega$$
$$= \frac{1}{\int_{\Omega^e} \mathrm{d}\Omega} \left(\int_{\Omega^e} (b^e)^2 \, \mathrm{d}\Omega \right)^{-1} \left(\int_{\Omega^e} b^e \, \mathrm{d}\Omega \right)^2 \tag{34}$$

Using the assumed function (32) we first evaluate the following two terms to be used in (34):

$$\int_{\Omega^e} b^e \, \mathrm{d}\Omega = j \int_{-1}^{1} b^e \, \mathrm{d}\xi = j \int_{-1}^{1} (1-\xi^2)^n \, \mathrm{d}\xi = j \frac{\pi^{1/2} \Gamma(n+1)}{\Gamma\left(n+\frac{3}{2}\right)} \tag{35}$$

$$\int_{\Omega^e} (b^e)^2 \, \mathrm{d}\Omega = j \int_{-1}^{1} (b^e)^2 \, \mathrm{d}\xi = j \int_{-1}^{1} (1-\xi^2)^{2n} \, \mathrm{d}\xi = j \frac{\pi^{1/2} \Gamma(2n+1)}{\Gamma\left(2n+\frac{3}{2}\right)} \tag{36}$$

where $\Gamma(x) = \int_0^\infty t^{x-1} \mathrm{e}^{-t} \, \mathrm{d}t$, and '$n$' is the power of the assumed function that is obtained by equating (29) and (34). Substituting (35) and (36) into (34) and simplifying the expression, we get

$$\tau_{\text{avg}} = \frac{1}{\int_{\Omega^e} b^e \, \mathrm{d}\Omega} \left(\int_{\Omega^e} (b^e)^2 \, \mathrm{d}\Omega \right)^{-1} \left(\int_{\Omega^e} b^e \, \mathrm{d}\Omega \right)^2 = \frac{(1+2n)\pi \Gamma(n+1) \Gamma(2n+1.5)}{4^{n+1} \Gamma(n+1.5)^3} \tag{37}$$

Employing a numerical approach and equating the right-hand sides of (29) and (37), one can determine the value of n that when substituted in (32) yields the desired bubble function (Figure 2). Table I shows the values of n and τ as a function of Peclet number *Pe*. Table II

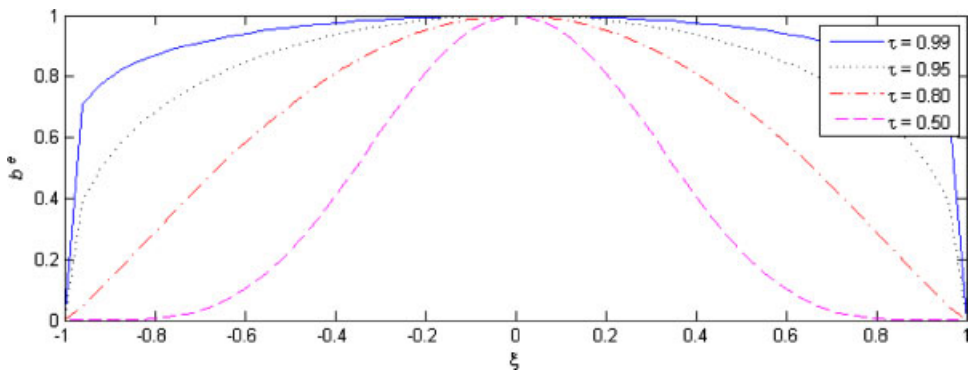

Figure 2. Bubble functions for various values of *Pe*.

DOI: 10.1002/fld

Table I. Value of n and stabilization parameter τ for various Pe.

Pe	4.50×10^6	441	216	81.0	36.0	13.5	6.00	2.25	0.00
n	0.001	0.136	0.205	0.373	0.630	1.210	2.000	3.184	5.123
τ	0.999999	0.990	0.980	0.950	0.900	0.800	0.700	0.600	0.500

Table II. Peclet number (Pe) and stability parameter (τ) as a function of $|\mathbf{a}|/\kappa$ and h.

	$\lvert\mathbf{a}\rvert/\kappa=10^0$		$\lvert\mathbf{a}\rvert/\kappa=10^2$		$\lvert\mathbf{a}\rvert/\kappa=10^4$		$\lvert\mathbf{a}\rvert/\kappa=10^6$	
h	Pe	τ	Pe	τ	Pe	τ	Pe	τ
0.05 (20×20 mesh)	0.05	0.5028	5	0.6786	500	0.9912	50 000	0.9999
0.025 (40×40 mesh)	0.025	0.5014	2.5	0.6087	250	0.9826	25 000	0.9998
0.0125 (80×80 mesh)	0.0125	0.5007	1.25	0.5610	125	0.9664	12 500	0.9996

presents stability parameter τ as a function of the Peclet number Pe. The initial slope of the curve at $Pe=0$ is $1/4a$. A value of $a=4.5$ has been used in the calculations (see Appendix B).

Remark 6
The slope of τ at $Pe=0$ is $1/4a$, where parameter $a>0$. The upper bound on parameter a is presented in Appendix B.

5. NUMERICAL RESULTS

This section presents a sequence of problems that investigate the stability and convergence properties of the proposed formulation. Figure 3 shows a family of linear and higher-order triangular and quadrilateral elements with equal-order pressure and velocity interpolations. Figure 4 shows the family of unequal-order triangular and quadrilateral elements where the linear-velocity quadratic-pressure and quadratic-velocity linear-pressure combinations are represented as $v1$–$p2$ and $v2$–$p1$, respectively. Appropriate numerical integration rules are employed for full integration. In all the convergence test cases presented in Sections 5.1–5.4, the underlying convective flow field is oriented at 30° with respect to the X-axis.

5.1. Convergence on regular meshes for equal-order elements

The first numerical simulation is a study of convergence rates. The domain under consideration is a biunit square, and the exact pressure solution is given by

$$p=\sin\frac{2\pi x}{L}\sin\frac{2\pi y}{L} \tag{38}$$

The velocity field is computed from Equation (1); φ is calculated from (2) by taking the divergence of the velocity field, and it is then integrated over domain to drive the problem.

DOI: 10.1002/fld

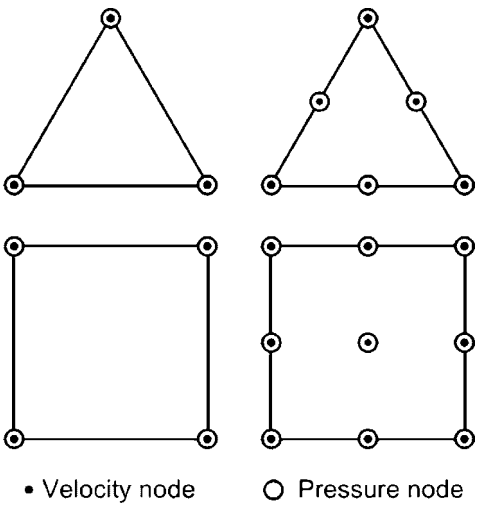

Figure 3. Family of continuous equal-order elements.

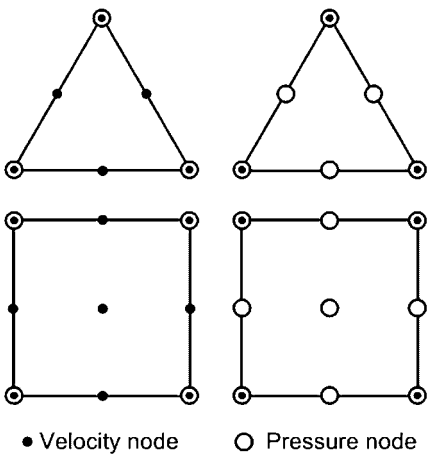

Figure 4. Family of continuous unequal-order elements.

The first set of tests present numerical convergence rates of the formulation over regular grids. Representative meshes for triangular and quadrilateral elements are shown in Figure 5(a)–(d). Finer meshes are constructed by uniformly dividing the elements, and the same pattern of element layout is maintained for linear and quadratic triangular and quadrilateral elements. We have plotted convergence of the velocity and pressure fields in the $L_2\mathbf{v}$, $L_2-\operatorname{div}\mathbf{v}$, $L_2 p$ and $H^1 p$ norms.

Table III presents values of τ that are a function of the physical constants of the problem '$|\boldsymbol{\alpha}|/\kappa$' and the characteristic length scale 'h' of the mesh as presented in Section 4.4. It can be seen that

DOI: 10.1002/fld

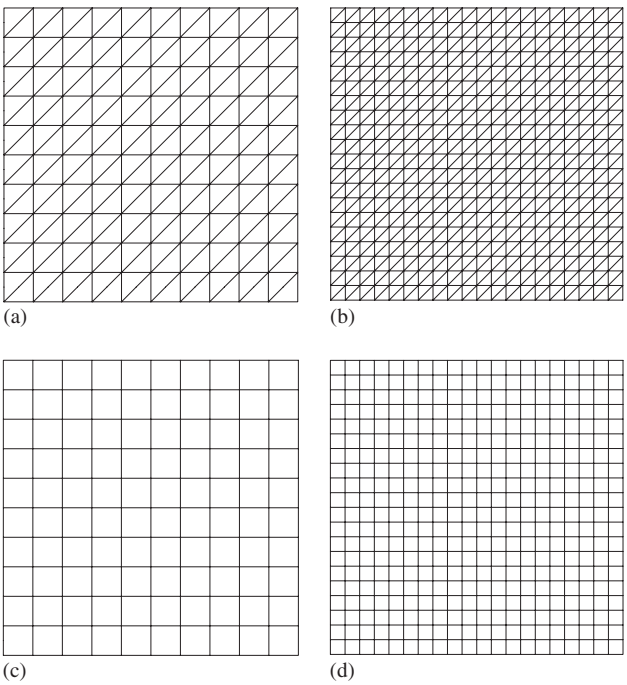

Figure 5. Uniform meshes for convergence study: (a) 200 triangular element mesh; (b) 800 triangular element mesh; (c) 100 quadrilateral element mesh; and (d) 400 quadrilateral element mesh.

Table III. Variation in the value of τ as a function of mesh refinement ($|\boldsymbol{\alpha}|/\kappa = 112$).

Mesh (h)	5×5 ($\frac{1}{5}$)	10×10 ($\frac{1}{10}$)	20×20 ($\frac{1}{20}$)	40×40 ($\frac{1}{40}$)	80×80 ($\frac{1}{80}$)
τ	0.8645	0.7867	0.7071	0.6258	0.5719

for given physical coefficients as the mesh is refined, element Peclet number decreases, and that results in a decrease in the value of stabilization parameter τ. This is a feature that is common with the stabilization parameters for the second-order form of the advection–diffusion equation presented in Hughes *et al.* [7], Franca *et al.* [10], Harari *et al.* [36], which scale as $O(h/|\boldsymbol{\alpha}|)$ in the advection-dominated cases.

Figure 6(a)–(d) presents numerical convergence rates on regular meshes for equal-order continuous-field elements for $|\boldsymbol{\alpha}|/\kappa = 1.41$, and this corresponds to the low Peclet number case. Similarly, Figure 7(a)–(d) presents numerical convergence study for $|\boldsymbol{\alpha}|/\kappa = 112$, and this corresponds to the high Peclet number case. In all the test cases, the convergence rates for $L_2 p$ and $H^1 p$ are optimal in the norms considered. Convergence rates for $L_2 \mathbf{v}$ and $L_2 - \operatorname{div} \mathbf{v}$ for the 3-node triangles and 4-node quadrilaterals are optimal in the norms considered. However, rates for $L_2 \mathbf{v}$ and $L_2 - \operatorname{div} \mathbf{v}$ for the 6-node triangles and 9-node quadrilaterals are sub-optimal, i.e. they are one order less as compared with their corresponding norms.

DOI: 10.1002/fld

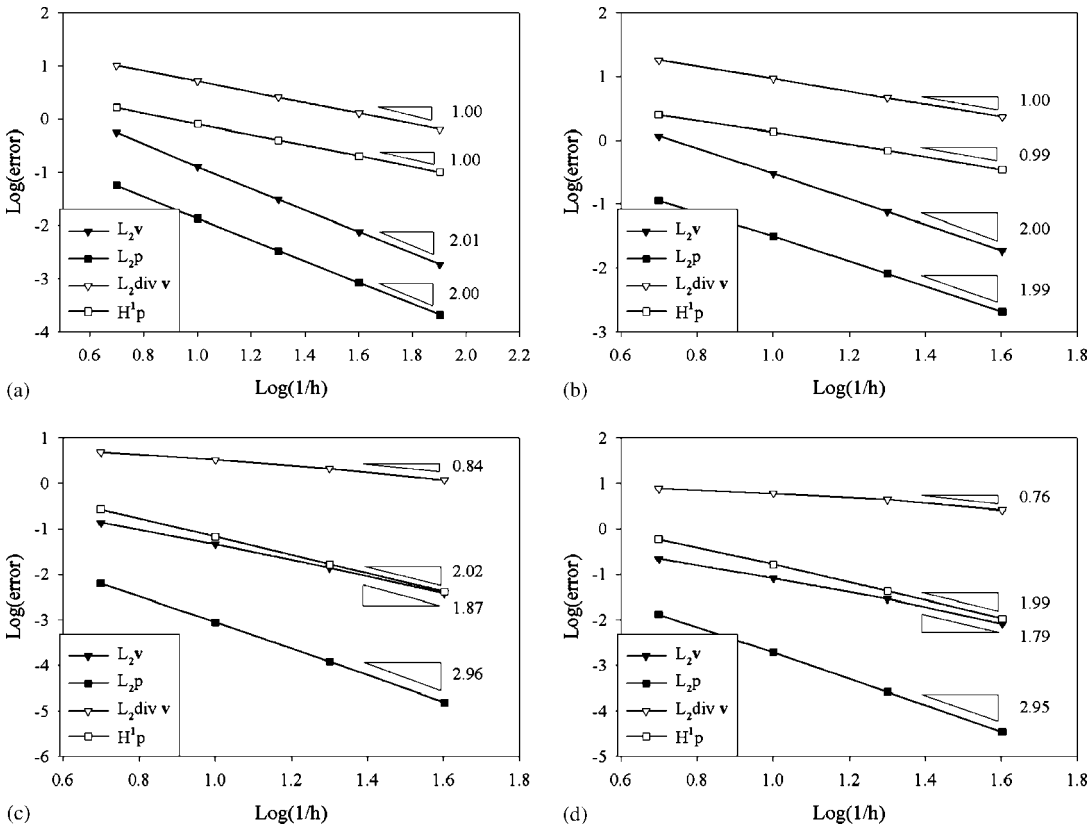

Figure 6. Convergence rates on regular meshes for equal-order continuous-field elements ($|\boldsymbol{\alpha}|/\kappa = 1.41$): (a) equal-order bilinear quads; (b) equal-order linear triangles; (c) equal-order biquadratic quads; and (d) equal-order quadratic triangles.

5.2. *Convergence on regular meshes for unequal-order elements*

This section shows convergence rates for unequal-order continuous-field elements on regular meshes shown in Figure 5. Linear-velocity quadratic-pressure and quadratic-velocity linear-pressure combinations are indicated as $v1$–$p2$ and $v2$–$p1$, respectively. Figures 8 and 9 present convergence rates for $|\boldsymbol{\alpha}|/\kappa = 1.41$ and 112 that correspond to low and high Peclet numbers, respectively. Linear-velocity quadratic-pressure ($v1$–$p2$) combination for both element types result in optimal convergence rates for all the norms considered. On the other hand, quadratic-velocity linear-pressure ($v2$–$p1$) combination for both element types results in convergence rates for $L_2 p$ and $H^1 p$ that are optimal in the norms considered. However, rates for $L_2\mathbf{v}$ and $L_2 - \operatorname{div}\mathbf{v}$ are sub-optimal, i.e. they are one order less compared with their corresponding norms.

5.3. *Convergence on unstructured and graded meshes*

This section presents convergence rates on unstructured and graded meshes. For the finer triangular meshes, the layout of the elements is maintained during successive mesh refinements shown in

DOI: 10.1002/fld

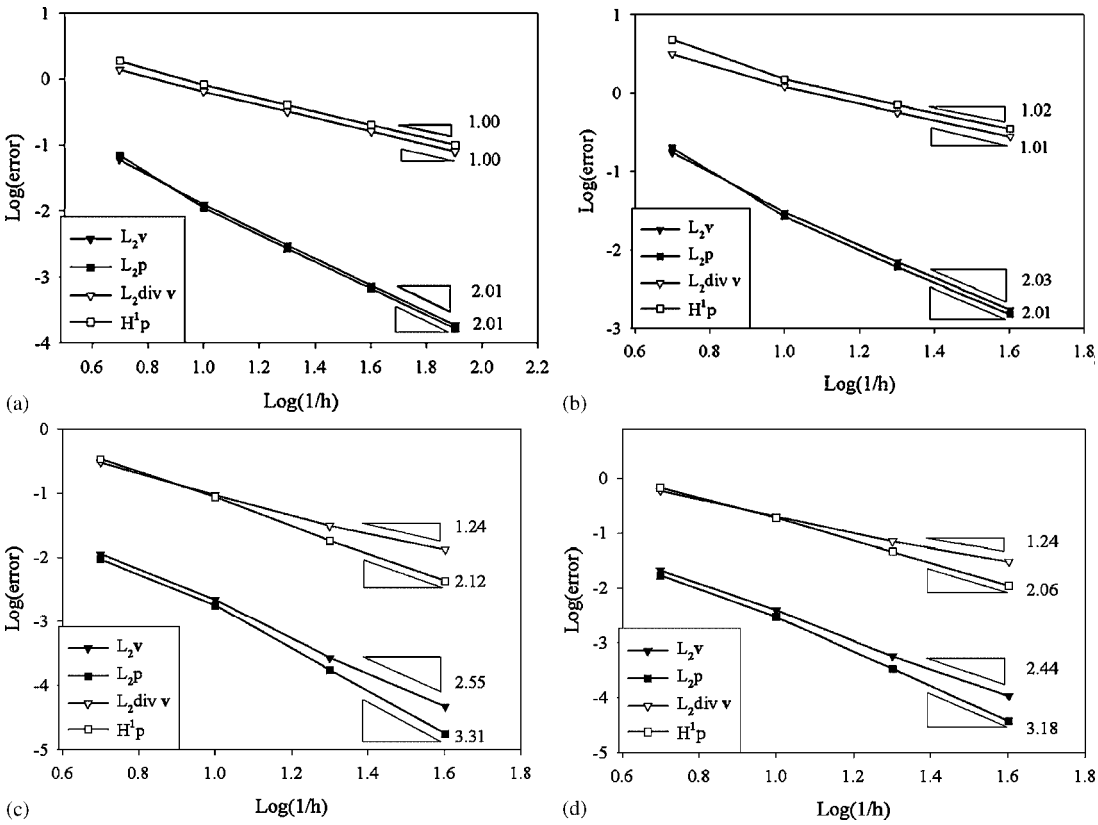

Figure 7. Convergence rates on regular meshes for equal-order continuous-field elements ($|\boldsymbol{\alpha}|/\kappa = 112$): (a) equal-order bilinear quads; (b) equal-order linear triangles; (c) equal-order biquadratic quads; and (d) equal-order quadratic triangles.

Figure 10(a) and (b). The finer quadrilateral meshes are constructed by uniformly bisecting the underlying elements in the coarse meshes shown in Figure 10(c) and (d).

Figure 11 presents the convergence rates for equal-order pressure–velocity elements for $|\boldsymbol{\alpha}|/\kappa = 112$ on unstructured meshes shown in Figure 10. In all the test cases, the convergence rates for $L_2\mathbf{v}$, $L_2 p$, $L_2 - \mathrm{div}\,\mathbf{v}$ and $H^1 p$ are nearly optimal in the norms considered. Similar trends in convergence rates are observed for the low Peclet number case, i.e. $|\boldsymbol{\alpha}|/\kappa = 1.41$, and are therefore not shown here.

5.4. *Convergence on composite meshes*

Figure 12 shows composite meshes that are developed by combining linear triangles and bilinear quadrilaterals, and quadratic triangles and biquadratic quadrilaterals in the same computational domain. Figures 13 and 14 present convergence rates for equal-order continuous-field elements for $|\boldsymbol{\alpha}|/\kappa = 1.41$ and 112, respectively. In all the test cases, the convergence rates for $L_2 p$ and $H^1 p$ are optimal in the norms considered. Convergence rates for $L_2\mathbf{v}$ and $L_2 - \mathrm{div}\,\mathbf{v}$ for the linear meshes

DOI: 10.1002/fld

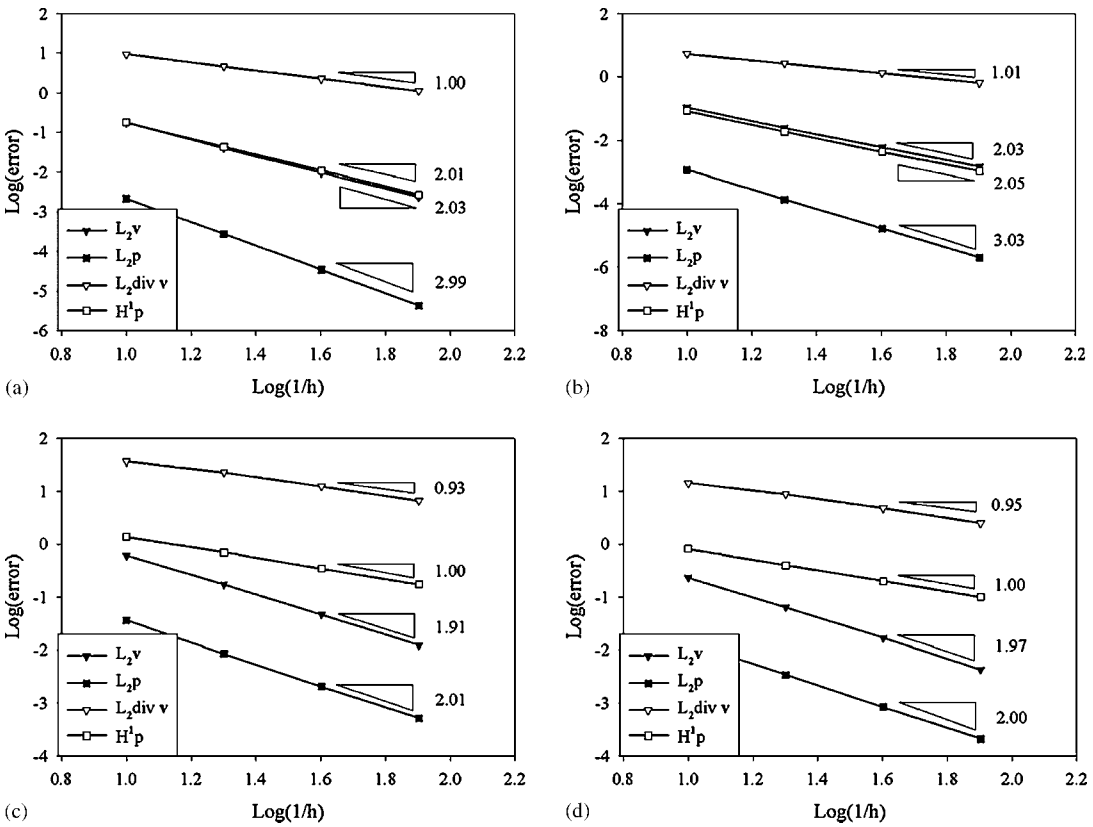

Figure 8. Convergence rates on regular meshes for unequal-order continuous-field elements ($|\boldsymbol{\alpha}|/\kappa = 1.41$). (a) 6-node triangles: $v1$–$p2$; (b) 9-node quadrilaterals: $v1$–$p2$; (c) 6-node triangles: $v2$–$p1$; and (d) 9-node quadrilaterals: $v2$–$p1$.

are optimal in the norms considered. However, rates for $L_2\mathbf{v}$ and $L_2 - \operatorname{div}\mathbf{v}$ for the quadratic meshes are sub-optimal, i.e. they are one order less compared with their corresponding norms.

5.5. *The five-spot problem*

The five-spot problem is a mathematically rough problem with prescribed velocity at the source and sink. The lower left corner represents the source whereas the upper right corner represents the sink (see Figure 15). Owing to symmetry of the five-spot problem, zero normal flow is prescribed along the boundaries. We assumed that the divergence of the velocity field φ consists of Dirac delta functions acting at source and sink locations, with strength $+\frac{1}{4}$ and $-\frac{1}{4}$, respectively. We calculated an equivalent distribution of normal velocity ψ and drove the problem with ψ, setting $\varphi = 0$. In the case of linear velocity elements, we assumed a linear distribution of ψ along the external edges of the corner elements, which is zero at the nodes adjacent to the corner nodes. This uniquely determines the distribution of ψ on the edge (see Figure 16(a)). In the case of

DOI: 10.1002/fld

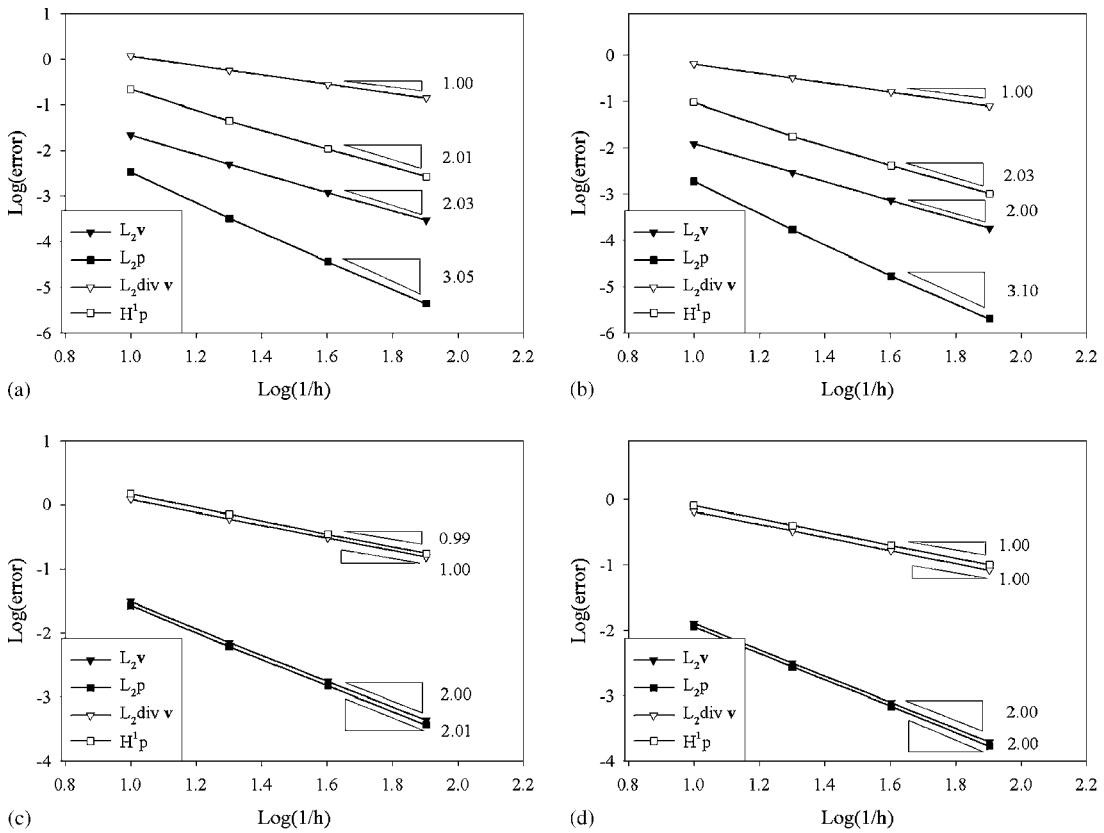

Figure 9. Convergence rates on regular meshes for unequal-order continuous-field elements ($|\boldsymbol{\alpha}|/\kappa = 112$). (a) 6-node triangles: $v1$–$p2$; (b) 9-node quadrilaterals: $v1$–$p2$; (c) 6-node triangles: $v2$–$p1$; and (d) 9-node quadrilaterals: $v2$–$p1$.

quadratic velocity elements, we assumed a parabolic distribution along the external edges of the corner elements, which is zero, and has zero derivative at the element vertex nodes away from the corner. Again, this uniquely defines the distribution of ψ along the edge (see Figure 16(b)).

In this problem, the convective flow field $\boldsymbol{\alpha}$ is directed along 45° with respect to the X-axis, i.e. along the main diagonal from source to sink. Figure 17(a) and (b) presents the computed pressure field for 4-node continuous-field elements.

5.6. The five-spot problem on checkerboard domain

This simulation tests the formulation for cases in which there are abrupt changes in the coefficients associated with a checkerboard domain. We consider the five-spot problem described earlier, now zoned as shown in Figure 18. Figure 19(a) shows pressures for $|\boldsymbol{\alpha}|/\kappa = 1.41$ in zones I and IV, and $|\boldsymbol{\alpha}|/\kappa = 14.1$ in zones II and III, for continuous-field, bilinear, equal-order quadrilaterals. Similarly,

DOI: 10.1002/fld

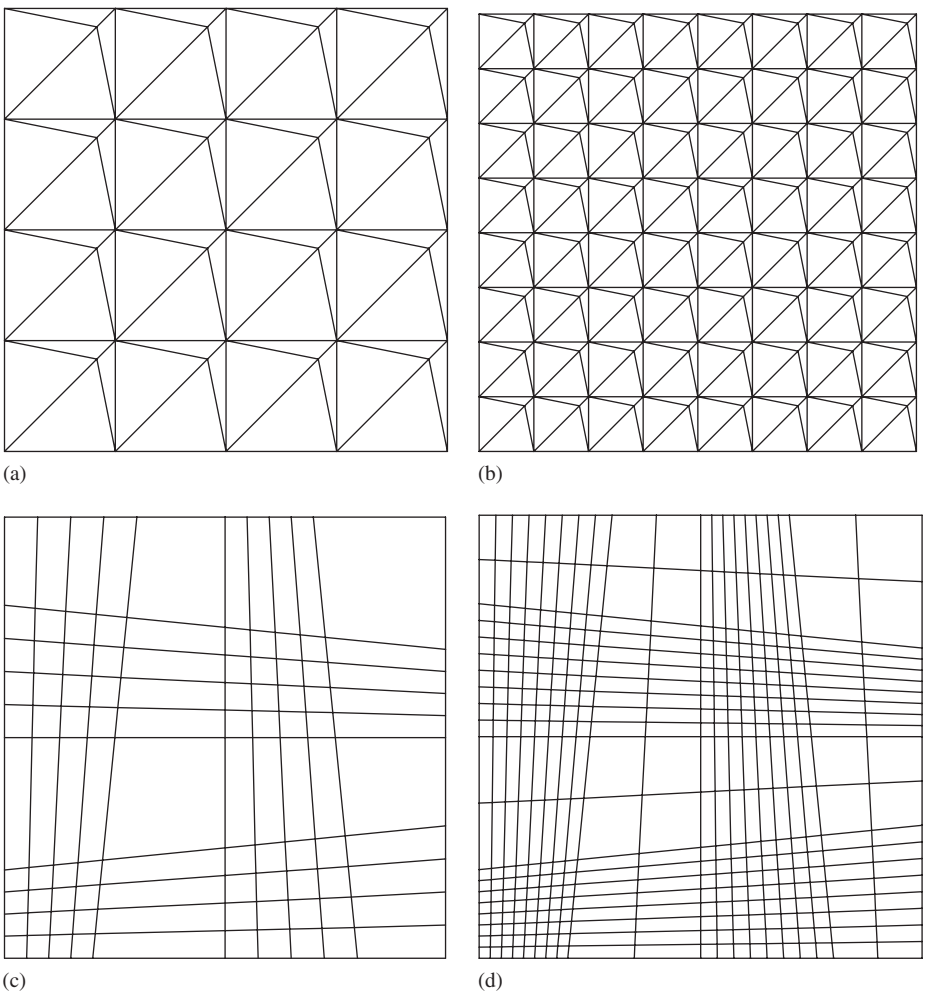

Figure 10. Unstructured meshes used for convergence study: (a) coarse triangular mesh; (b) fine triangular mesh; (c) coarse quadrilateral mesh; and (d) fine quadrilateral mesh.

Figure 19(b) shows pressures for $|\boldsymbol{\alpha}|/\kappa = 1.41$ in zones I and IV, and $|\boldsymbol{\alpha}|/\kappa = 141$ in zones II and III. In both the cases there are no oscillations in the pressure field, an indication of robustness.

5.7. Advection in a rotating flow field

This problem tests the method for high Peclet number flows and is used to assess solutions that are essentially purely advective in nature. The problem is defined on a unit square of coordinates $-0.5 \leqslant x, y \leqslant 0.5$, where the flow velocity components are given by

$$a_1 = -y, \quad a_2 = x \tag{39}$$

DOI: 10.1002/fld

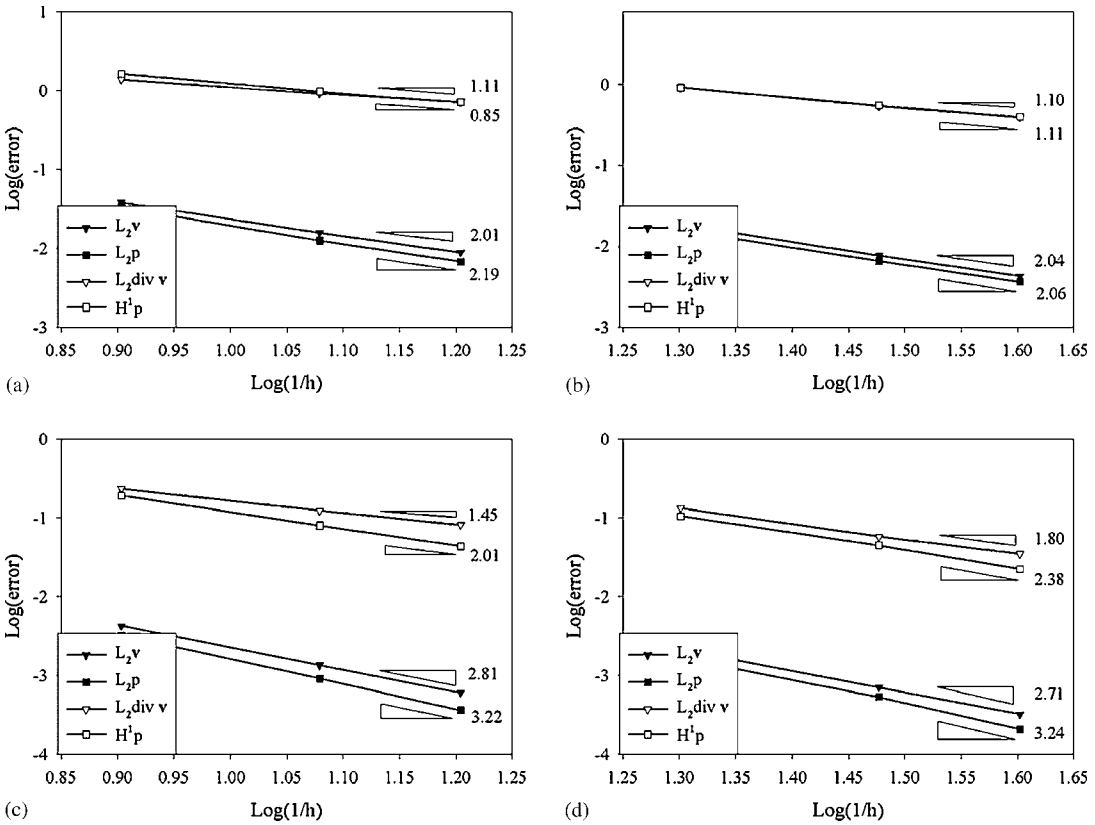

Figure 11. Convergence rates on unstructured–graded meshes for equal-order continuous-field elements ($|\boldsymbol{\alpha}|/\kappa = 112$): (a) equal-order linear triangles; (b) equal-order bilinear quads; (c) equal-order quadratic triangles; and (d) equal-order biquadratic quads.

Along the external boundary pressure and normal velocity are zero. Along the internal boundary (OA) pressure profile is

$$p = \tfrac{1}{2}(\cos(4\pi y + \pi) + 1), \quad -0.5 \leqslant y \leqslant 0 \tag{40}$$

A schematic diagram of the problem statement is shown in Figure 20.

The diffusivity is $\kappa = 10^{-6}$. A uniform mesh with 30×30 equal-order 4-node elements is employed. Figure 21(a) shows the elevation plots for the GLS method that is obtained via the second-order form of the advection–diffusion equation, and Figure 21(b) shows the elevation plot for the present method. This problem has a *smooth* exact solution and therefore both methods perform well. Elevation plot for the equal-order 3-node triangles is shown in Figure 22(a). For the lower-order elements, i.e. 4-node quadrilaterals (Figure 21(b)) and 3-node triangles (Figure 22(a)), there are small oscillations that disappear as the order of the polynomials is increased, e.g. 9-node equal-order quadrilaterals shown in Figure 22(b). A similar smooth profile was attained for the 6-node equal-order triangles and is therefore not presented here.

DOI: 10.1002/fld

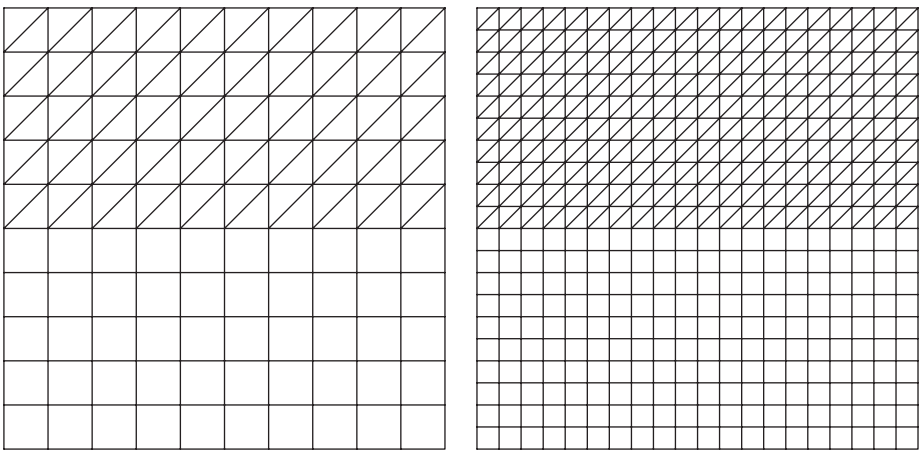

Figure 12. Composite meshes used for convergence study.

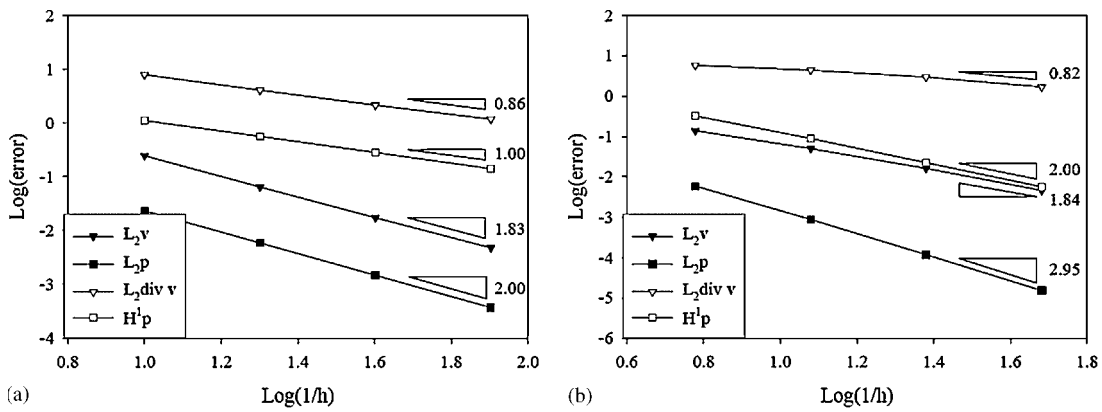

Figure 13. Convergence rates on composite meshes for equal-order continuous-field elements ($|\boldsymbol{\alpha}|/\kappa = 1.41$): (a) equal-order bilinear quads and triangles and (b) equal-order biquadratic quads and triangles.

5.8. Advection skew to the mesh

This numerical simulation is also a standard benchmark problem for high Peclet number flows. It is a rough numerical test in that various layers are present in the exact solution. In this problem a discontinuity in the data at the boundary is propagated into the domain, which creates an internal layer. Domain under consideration is a biunit square and uniform meshes with 30×30 and 40×40 equal-order 4-node quadrilateral elements are used. In addition, the problem is subjected to homogeneous essential boundary conditions at the outflow boundary, which gives rise to outflow boundary layers (see Figure 23 for the problem statement). We consider diffusivity $\kappa = 1 \times 10^{-2}$ that yields a Peclet number $Pe = uL_y/\kappa = 100$ for this flow. Results for $\theta = \arctan = 1.0$ for the proposed method for the 4-node quadrilaterals are shown in Figure 24(a) and (b), respectively.

DOI: 10.1002/fld

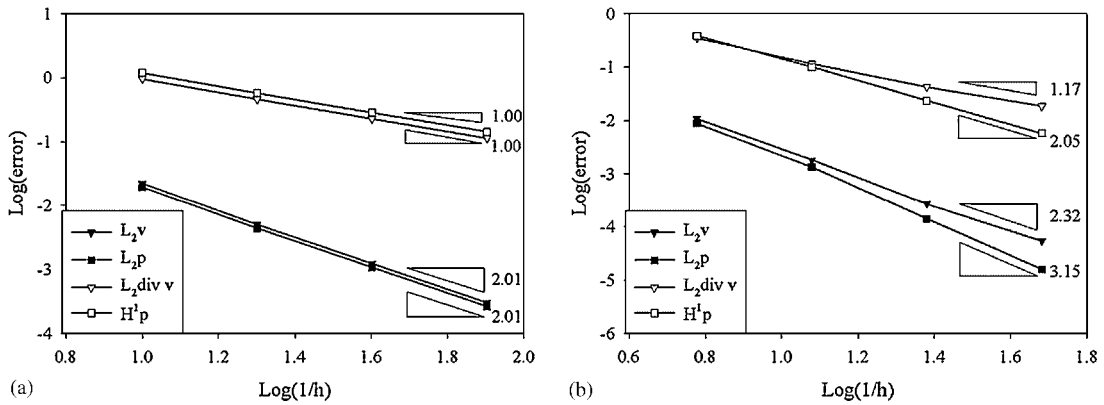

Figure 14. Convergence rates on composite meshes for equal-order continuous-field elements ($|\boldsymbol{\alpha}|/\kappa = 112$): (a) equal-order bilinear quads and triangles and (b) equal-order biquadratic quads and triangles.

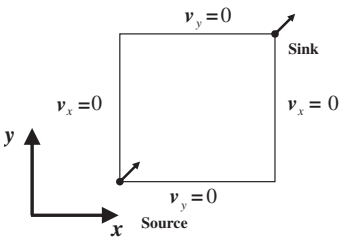

Figure 15. Problem with point source and sink, commonly called the five-spot problem.

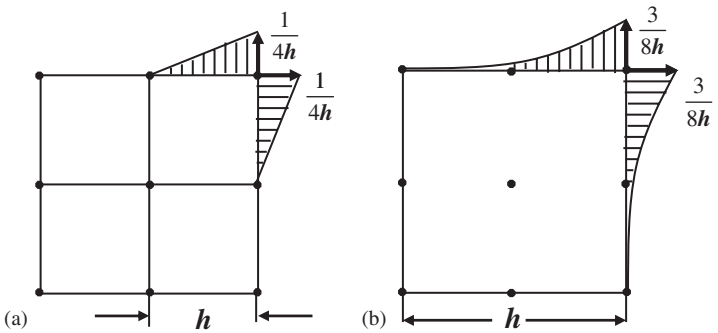

Figure 16. (a, b) Distribution of ψ along the corner elements at the source. The distribution of ψ at the sink is the same with opposite sign.

DOI: 10.1002/fld

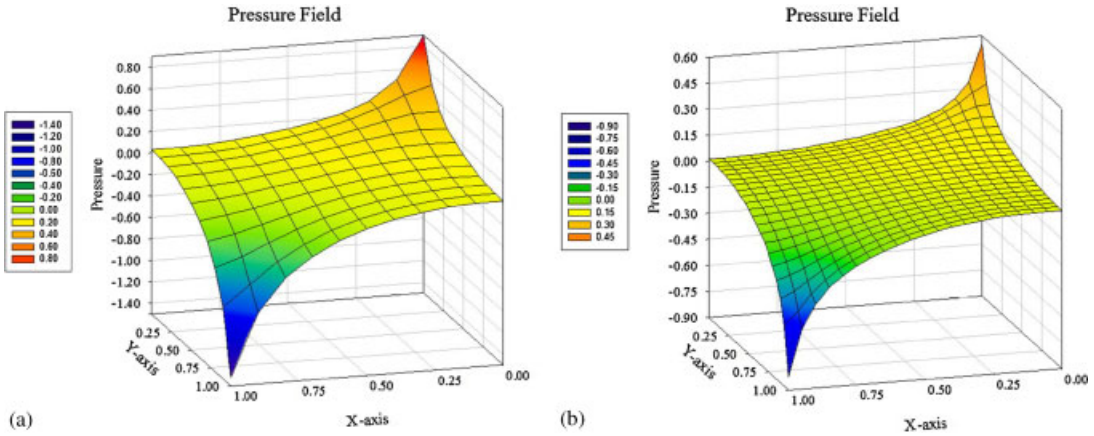

Figure 17. Computed continuous pressure field for 4-node elements: (a) 100 4-node elements, $|\boldsymbol{\alpha}|/\kappa = 1.41$ and (b) 400 4-node elements, $|\boldsymbol{\alpha}|/\kappa = 1.41$.

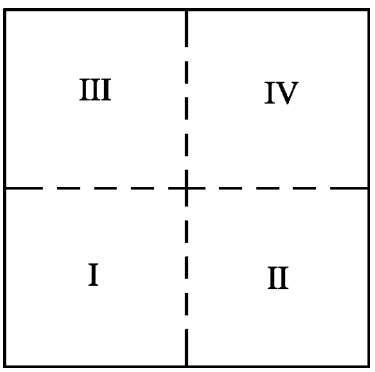

Figure 18. Checkerboard domain with discontinuous coefficients.

Note that all solutions present oscillations in the thin layer regions, as expected from local error analysis and numerical results presented in [36]. In these problems, results for the Galerkin method are highly oscillatory and consequently they are not shown here. Similarly, Figure 25(a) and (b) present the results for the equal-order 9-node quadrilaterals.

6. CONCLUDING REMARKS

We have presented a new stabilized finite element method for the first-order form of the advection–diffusion equation. The new stabilized form is derived based on an overlapping sum decomposition of the velocity field into coarse- and fine-scale components. Solution of the fine-scale problem is variationally embedded in the coarse-scale problem and this step also yields the structure of the stabilization parameter. The key ingredient in the formulation is a volumetric, residual-based,

DOI: 10.1002/fld

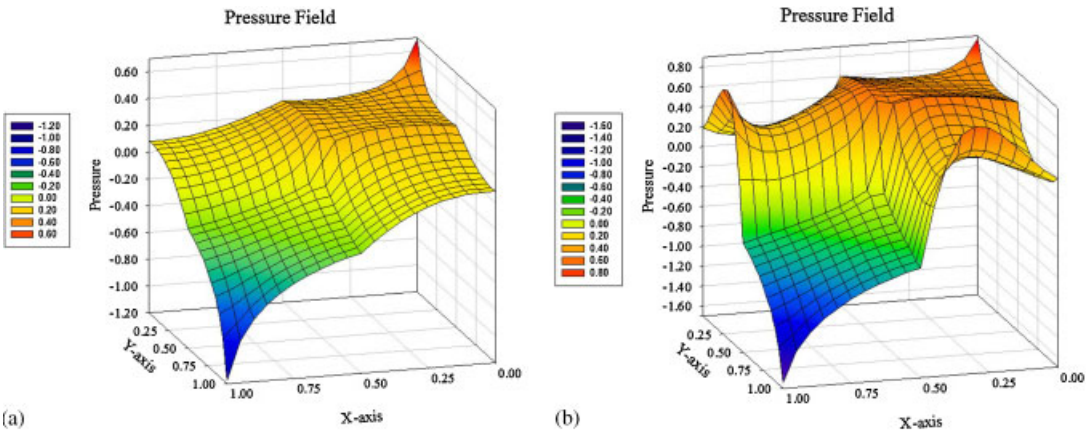

Figure 19. Computed continuous pressure for the checkerboard domain: (a) Zone I, IV: $|\boldsymbol{\alpha}|/\kappa = 1.41$ Zone II, III: $|\boldsymbol{\alpha}|/\kappa = 14.1$ and (b) Zone I, IV: $|\boldsymbol{\alpha}|/\kappa = 1.41$ Zone II, III: $|\boldsymbol{\alpha}|/\kappa = 141$.

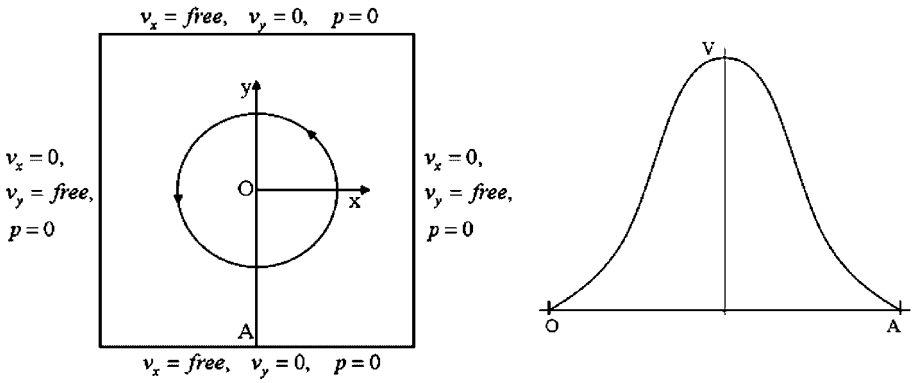

Figure 20. Schematic diagram of the problem.

stabilization term that is free of an explicit appearance of the characteristic length scales of the mesh. We perform fairly extensive numerical tests involving two-dimensional equal-order and unequal-order velocity–pressure elements. Linear and quadratic triangles and quadrilaterals are tested for structured as well as for distorted and unstructured meshes. The new formulation is convergent for all combinations of continuous pressure and continuous velocity interpolations. For lower-order elements, optimal convergence rates are attained for $L_2\mathbf{v}$, $L_2 - \operatorname{div}\mathbf{v}$, $L_2 p$ and $H^1 p$ in the norms considered. For all equal- and unequal-order combinations in the higher-order elements, optimal convergence rates are attained for $L_2 p$ and $H^1 p$ in the norms considered. However, convergence rates for the velocity in $L_2\mathbf{v}$ and its divergence in $L_2 - \operatorname{div}\mathbf{v}$ are one order less than their corresponding norms. We also perform several tests of robustness involving elliptic singularities (the five-spot problem) and discontinuous coefficients associated with a checkerboard domain. Two test cases of high Peclet number flows, one with a smooth solution and the other

DOI: 10.1002/fld

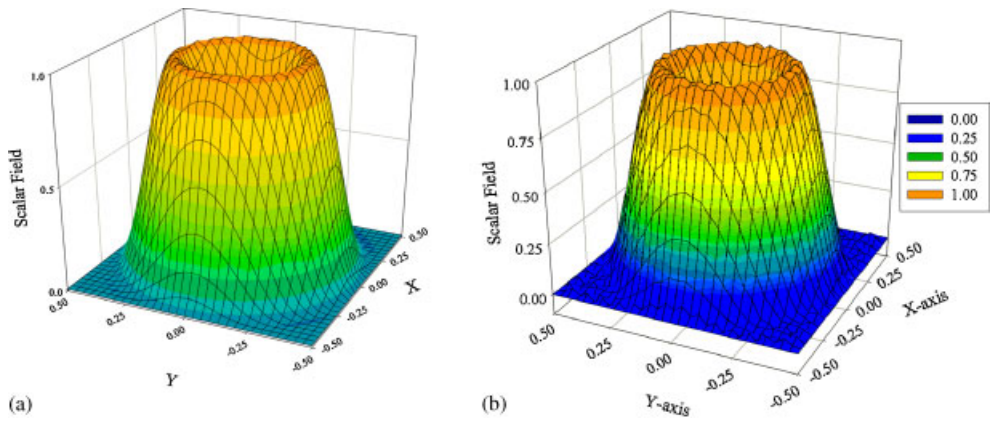

Figure 21. Computed pressure field for the rotating hill problem: (a) 900 4-node element mesh (GLS method) and (b) 900 4-node element mesh (present method).

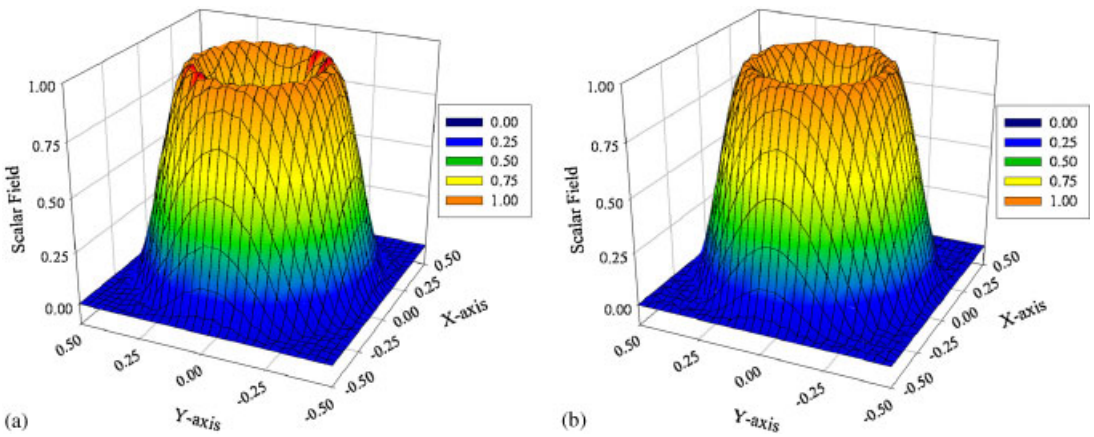

Figure 22. Computed pressure field for the rotating hill problem (various element types): (a) 1800 3-node element mesh (present method) and (b) 225 9-node element mesh (present method).

with sharp layers, are also carried out, which are an indicator of the robustness of the proposed method.

APPENDIX A: FIRST-ORDER FORM OF THE ADVECTION–DIFFUSION EQUATION

The advection–diffusion equation is typically written in the second-order form as

$$\boldsymbol{\alpha}\cdot\nabla p-\kappa\Delta p=\varphi \quad \text{on } \Omega \tag{A1}$$

DOI: 10.1002/fld

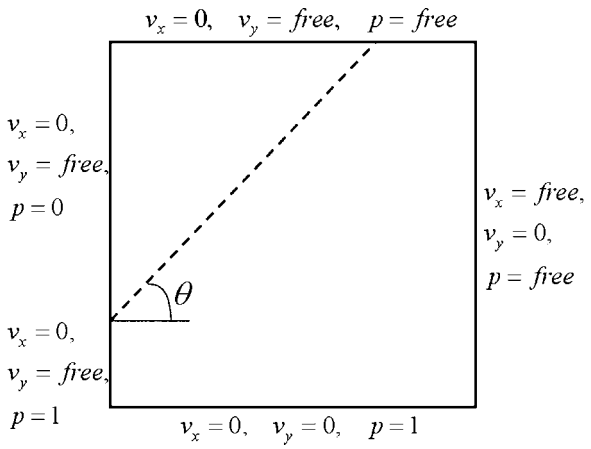

Figure 23. Schematic diagram of the problem.

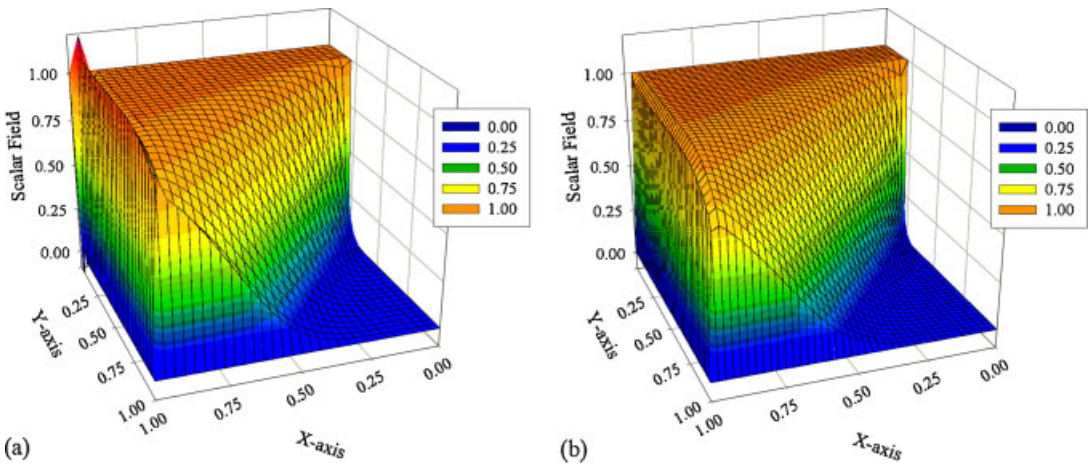

Figure 24. Computed pressure field for the skew advection problem (4-node quadrilaterals): (a) advection skew to the mesh for arctan 1 (900 4-node element mesh) and (b) advection skew to the mesh for arctan 1 (1600 4-node element mesh).

where p is the unknown scalar field, $\boldsymbol{\alpha}(\mathbf{x})$ is the given flow velocity that is assumed solenoidal, i.e. $\nabla \cdot \boldsymbol{\alpha} = 0$ in Ω, $\kappa = \kappa(x) > 0$ represents diffusivity, and $\varphi(\mathbf{x})$ is the prescribed source function. Introducing $\mathbf{v} = \boldsymbol{\alpha} p - \kappa \nabla p$, (A1) can be written as

$$\mathbf{v} = \boldsymbol{\alpha} p - \kappa \nabla p \quad \text{on } \Omega \tag{A2}$$

$$\operatorname{div} \mathbf{v} = \varphi \quad \text{on } \Omega \tag{A3}$$

The set of equations (A2) and (A3) also represent convective–diffusive heat transfer wherein p represents the temperature field and $\mathbf{v}$ represents the temperature-flux field.

DOI: 10.1002/fld

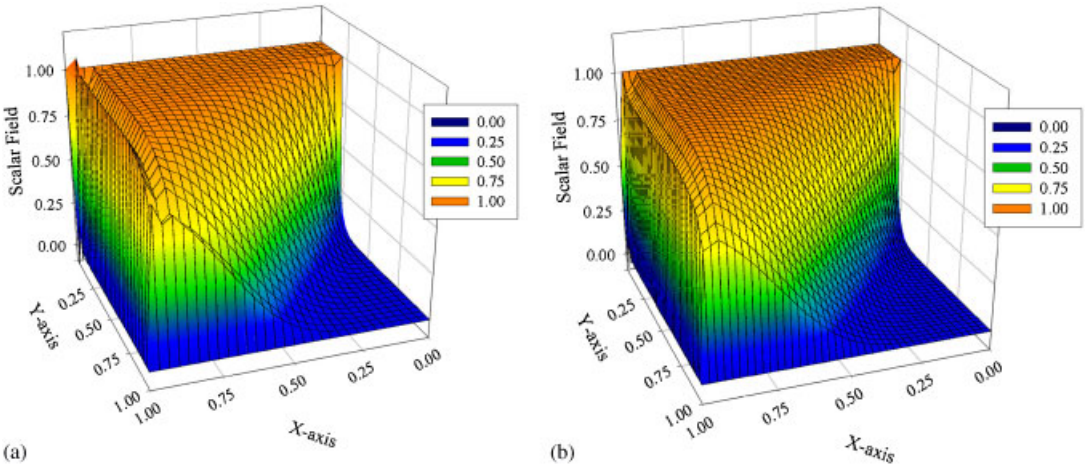

Figure 25. Computed pressure field for the skew advection problem (9-node quadrilaterals): (a) advection skew to the mesh for arctan 1 (225 9-node element mesh) and (b) advection skew to the mesh for arctan 1 (400 9-node element mesh).

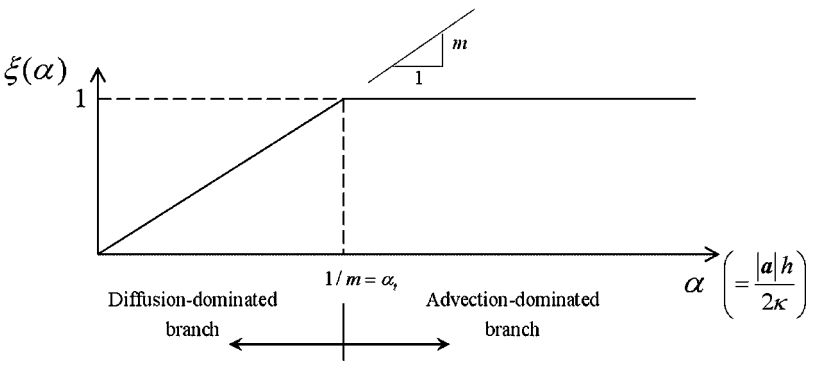

Figure B1. Definition of $\zeta(\alpha)$.

APPENDIX B: DETERMINATION OF THE UPPER BOUND ON THE INITIAL SLOPE FOR τ *VERSUS* *Pe* CURVE

In GLS method for advection-diffusive equation presented in Hughes *et al.* [7], the definition of stability parameter is given as $\tau=\frac{1}{2}(h/|\mathbf{a}|)\xi(\alpha)$, where the function $\zeta(\alpha)$ is shown in Figure B1. The transition Peclet number $\alpha_t=1/m\geqslant c^2/4$, where c is the constant in the inverse estimate presented in Hughes *et al.* [7].

We employ this idea to obtain a smooth τ *versus* *Pe* curve with a value of $\tau=0.5$ at $Pe=0$ (which is the Darcy limit given in [24]) and it asymptotes to $\tau\simeq 1$ in the advection-dominated case. We set $Pe_t=2\alpha_t\geqslant c^2/2$ as the transition point between diffusion and advection-dominated branches as shown in Figure B2.

DOI: 10.1002/fld

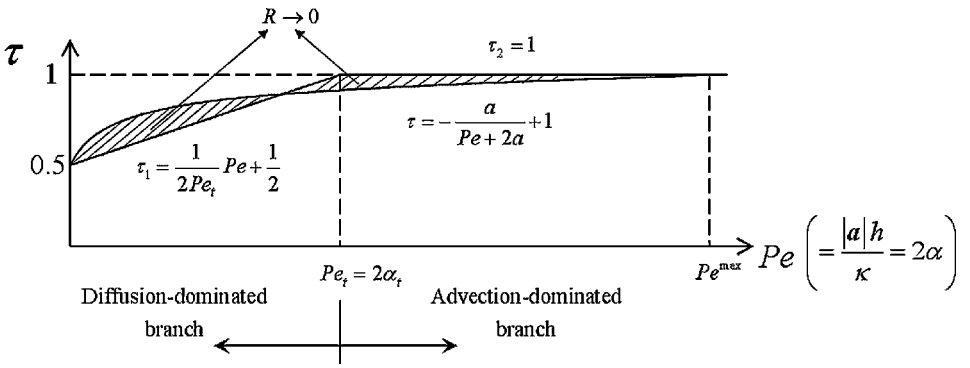

Figure B2. Design condition for the initial slope for the smooth τ *versus Pe* curve.

The design condition for the parameter 'a' that defines the initial slope of τ *versus Pe* curve employed in the design of the bubble function (presented in Section 4.4) is obtained in the limit as the residual R approaches zero. Let $Pe^{\max}$ represent a sufficiently high Peclet number. We want

$$R=\int_0^{Pe_t}(\tau_1-\tau)\,\mathrm{d}Pe+\int_{Pe_t}^{Pe^{\max}}(\tau_2-\tau)\,\mathrm{d}Pe\to 0 \tag{B1}$$

where $\tau=-a/(Pe+2a)+1$, $\tau_1=(1/(2Pe_t))Pe+\frac{1}{2}$, and $\tau_2=1$.

$$\begin{aligned}R&=\int_0^{Pe_t}\left(\frac{1}{2Pe_t}Pe+\frac{1}{2}+\frac{a}{Pe+2a}-1\right)\mathrm{d}Pe+\int_{Pe_t}^{Pe^{\max}}\left(1+\frac{a}{Pe+2a}-1\right)\mathrm{d}Pe\\&=\left[\frac{1}{4Pe_t}Pe^2-\frac{1}{2}Pe\right]_0^{Pe_t}+[a\ln(Pe+2a)]_0^{Pe^{\max}}\\&=\frac{Pe_t}{4}-\frac{Pe_t}{2}+a\ln\left(\frac{Pe^{\max}+2a}{2a}\right)\\&\cong-\frac{Pe_t}{4}+a\ln(Pe^{\max})\end{aligned} \tag{B2}$$

Using a high enough Peclet number (say $Pe^{\max}=10^3$) and setting (B2) equal to zero, we get

$$a=\frac{Pe_t}{4}\frac{1}{\ln(Pe^{\max})}=\frac{Pe_t}{27.63}\geqslant\frac{c^2}{55.26} \tag{B3}$$

where we have used $Pe_t=2\alpha_t\geqslant c^2/2$. This yields the initial slope of the curve defined as $1/4a$:

$$\text{The initial slope}=\frac{1}{4a}\leqslant\frac{13.815}{c^2} \tag{B4}$$

where 'c' is the constant in the inverse estimate presented in [7].

DOI: 10.1002/fld

ACKNOWLEDGEMENTS

This work was partially supported by the National Academy of Sciences Grant NAS 7251-05-005. This support is gratefully acknowledged.

REFERENCES

1. Franca LP, Farhat C. Bubble functions prompt unusual stabilized finite element methods. *Computer Methods in Applied Mechanics and Engineering* 1995; **123**:299–308.
2. Franca LP, Frey SL, Hughes TJR. Stabilized finite element methods: I. Application to the advective–diffusive model. *Computer Methods in Applied Mechanics and Engineering* 1992; **95**:253–276.
3. Franca LP, Nesliturk A, Stynes M. On the stability of residual-free bubbles for convection–diffusion problems and their approximation by a two-level finite element method. *Computer Methods in Applied Mechanics and Engineering* 1998; **166**:35–49.
4. Hughes TJR, Brooks AN. Streamline-upwind/Petrov–Galerkin methods for advection dominated flows. *Proceedings of the Third International Conference on Finite Element Methods in Fluid Flow*, Banff, June 1980; 283–292.
5. Masud A, Khurram R. A multiscale/stabilized finite element method for the advection–diffusion equation. *Computer Methods in Applied Mechanics and Engineering* 2004; **193**:1997–2018.
6. Tezduyar TE, Park YJ. Discontinuity-capturing finite element formulations for nonlinear convection–diffusion–reaction equations. *Computer Methods in Applied Mechanics and Engineering* 1986; **59**:307–325.
7. Hughes TJR, Franca LP, Hulbert GM. A new finite element formulation for computational fluid dynamics: VIII. The Galerkin-least-squares method for advective–diffusive equations. *Computer Methods in Applied Mechanics and Engineering* 1989; **73**:173–189.
8. Palaniappan J, Haber RB, Jerrard RL. A space-time discontinuous Galerkin method for scalar conservation laws. *Computer Methods in Applied Mechanics and Engineering* 2004; **193**:3607–3631.
9. Baumann CE, Oden JT. A discontinuous hp finite element method for convection–diffusion problems. *Computer Methods in Applied Mechanics and Engineering* 1999; **175**:311–341.
10. Franca LP, Hauke G, Masud A. Revisiting stabilized finite element methods for the advective–diffusive equation. *Computer Methods in Applied Mechanics and Engineering* 2006; **195**:1560–1572.
11. Ayub M, Masud A. A new stabilized formulation for convective–diffusive heat transfer. *Numerical Heat Transfer* 2003; **43**(6):601–625.
12. Rajagopal KR. On a hierarchy of approximate models for flows of incompressible fluids through porous solids. *Mathematical Models and Methods in Applied Sciences* 2007; **17**(2):215–252.
13. Fiard JM, Manteuffel TA, McCornick SF. First-order system least squares (FOSLS) for convection–diffusion problems: numerical results. *SIAM Journal on Scientific Computing* 1998; **19**(6):1958–1979.
14. Babuska I. Error bounds for finite element methods. *Numerische Mathematik* 1971; **16**:322–333.
15. Brezzi F. On the existence, uniqueness and approximation of saddle point problems arising from Lagrangian multipliers. *RAIRO—Analyse Numerique* 1974; **8**:129–151.
16. Raviart PA, Thomas JM. A mixed finite element method for second order elliptic problems. In *Mathematical Aspects of the Finite Element Method*, Galligani I, Magenes E (eds). Lecture Notes in Mathematics, vol. 606. Springer: New York, 1977.
17. Brezzi F, Douglas J, Marini LD. Two families of mixed finite elements for second order elliptic problems. *Numerische Mathematik* 1985; **47**:217–235.
18. Brezzi F, Douglas J, Marini LD. Recent results on mixed finite elements for second order elliptic problems. In *Vistas in Applied Mathematics*, *Numerical Analysis*, *Atmospheric Sciences*, *Immunology*, Balakrishnan AV, Dorodnitsyn AA, Lions JL (eds). Optimization Software Publications: New York, 1986.
19. Brezzi F, Douglas J, Fortin M, Marini LD. Efficient rectangular mixed finite elements in two and three space variables. *Mathematical Modelling and Numerical Analysis* 1987; **21**:581–604.
20. Nedelec JC. Mixed finite elements in R3. *Numerische Mathematik* 1980; **35**:315–341.
21. Nedelec JC. A new family of mixed finite elements in R3. *Numerische Mathematik* 1986; **50**:57–81.
22. Thomas JM. *Surl'analyse numerique des methodes d'elements finis hybrides et mixtes*. These d'Etat, Universite Pierre et Marie Curie, Paris, 1977.
23. Brooks AN, Hughes TJR. Streamline upwind/Petrov–Galerkin formulations for convection dominated flows with particular emphasis on the incompressible Navier–Stokes equations. *Computer Methods in Applied Mechanics and Engineering* 1982; **32**:199–259.

DOI: 10.1002/fld

24. Masud A, Hughes TJR. A stabilized mixed finite element method for Darcy flow. *Computer Methods in Applied Mechanics and Engineering* 2002; **191**:4341–4370.
25. Hughes TJR, Masud A, Wan J. A discontinuous-Galerkin finite element method for Darcy flow. *Computer Methods in Applied Mechanics and Engineering* 2006; **195**:3347–3381.
26. Brezzi F, Hughes TJR, Marini LD, Masud A. Mixed discontinuous Galerkin methods for Darcy flow. *SIAM Journal on Scientific Computing* 2005; **22**(1):119–145.
27. Masud A. A stabilized mixed finite element method for Darcy–Stokes flow. *International Journal for Numerical Methods in Fluids* 2007; **54**:665–681.
28. Hughes TJR. Multiscale phenomena: Green's functions, the Dirichlet-to-Neumann formulation, subgrid scale models, bubbles and the origin of stabilized methods. *Computer Methods in Applied Mechanics and Engineering* 1995; **127**:387–401.
29. Hughes TJR, Feijoo G, Mazzei L, Quincy JB. The variational multiscale method: a paradigm for computational mechanics. *Computer Methods in Applied Mechanics and Engineering* 1998; **166**:3–24.
30. Brezzi F, Fortin M. *Mixed and Hybrid Finite Element Methods*. Springer Series in Computational Mathematics, vol. 15. Springer: New York, 1991.
31. Farhat C, Harari I, Hetmaniuk U. A discontinuous Galerkin method with Lagrange multipliers for the solution of Helmholtz problems in the mid-frequency regime. *Computer Methods in Applied Mechanics and Engineering* 2003; **192**(11–12):1389–1419.
32. Brezzi F, Bristeau M, Franca L, Mallet M, Roge G. A relationship between stabilized finite element methods and the Galerkin method with bubble functions. *Computer Methods in Applied Mechanics and Engineering* 1992; **96**:117–129.
33. Brezzi F, Franca LP, Hughes TJR, Russo A. $b=\int g$. *Computer Methods in Applied Mechanics and Engineering* 1997; **145**:329–339.
34. Masud A, Franca LP. A hierarchical multiscale framework for problems with multiscale source terms. *Computer Methods in Applied Mechanics and Engineering* 2008. DOI: 10.1016/j.cma.2007.12.024.
35. Masud A, Khurram R. A multiscale finite element method for the incompressible Navier–Stokes equations. *Computer Methods in Applied Mechanics and Engineering* 2006; **195**:1750–1777.
36. Harari I, Franca LP, Oliveira SP. Streamline design of stability parameters for advection–diffusion problems. *Journal of Computational Physics* 2001; **171**:115–131.